Topological analysis of chaos in the optically pumped laser

R. Gilmore,[1] R. Vilaseca,[2] R. Corbalán,[3] and E. Roldán[4]
[1]*Department of Physics and Atmospheric Science, Drexel University, 32nd & Chestnut Street, Philadelphia, Pennsylvania 19104*
[2]*Departament de Fisica i Enginyeria Nuclear, Universitat Politècnica de Catalunya, Colom 11, E-08222 Terrassa, Spain*
[3]*Departament de Fisica, Universitat Autònoma de Barcelona, E-08193 Bellaterra, Spain*
[4]*Departament d'Optica, Universitat de València, Dr. Moliner 50, E-46100 Burjassot, Spain*
(Received 29 October 1996)

A topological analysis has been carried out on time series generated from a Doppler broadened three-level model, which has been proposed to describe optically pumped lasers, in particular the far-infrared ammonia laser. In certain parameter ranges it is known that the experimental findings and the predictions from the Doppler broadened optically pumped laser model closely agree and show features that follow the dynamics of the Lorenz model. By means of a suitable symmetry adapted differential phase space embedding, the present analysis shows that, in fact, the embedded data sets are topologically equivalent to the Lorenz attractor. This equivalence essentially remains upon variation of a laser control parameter within a certain range. [S1063-651X(97)07403-5]

PACS number(s): 05.45.+b, 42.65.Sf, 42.55.Lt

I. INTRODUCTION

Chaotic dynamics of a large variety of systems has been studied in recent years, often motivated by the wish to understand this ''unpredictable'' deterministic behavior in particular systems. Optics with its ready control of the degrees of freedom of a system has proved to be a fertile field for the study of low-dimensional chaotic dynamics [1]. It has proven to be also a fortunate field after the recognition [2] that a model describing a single-mode homogeneously broadened resonantly tuned ring laser is isomorphic to the Lorenz model [3], the simplest and most paradigmatic model, which exhibits chaos in an autonomous system.

However, the experimental observation in a laser system of the dynamics predicted by the Lorenz-Haken model turned out to be a long standing and challenging problem. Up to now this type of dynamics has been observed only on an optically pumped far-infrared ammonia laser [4,5]. This fact originated a controversy [6], since such a laser device is a relatively complex physical system involving factors such as coherent pumping and Doppler broadening, which make the number of degrees of freedom much larger than in the Lorenz model. In fact, a realistic laser model taking into account these two physical factors (Doppler broadened optically pumped laser model, DOPL [6–8]) has shown, in certain parameter ranges, results in remarkable agreement with the experimental findings and, at the same time, with Lorenz-model predictions.

Comparisons with the Lorenz model, however, have been performed so far only by visual and metric analysis: qualitative comparison of time series and bifurcation diagrams and calculation of spectra of generalized dimensions, entropy, and return maps of the laser intensity peak value [6–8].

Metric analysis (in particular, the determination of geometric quantities such as fractal dimensions, entropy, and Lyapunov exponents [9,10]), however, does not provide a full understanding or description of the system dynamics. Such analysis requires long, low noise data sets and generates real numbers, usually without error bars, which are difficult to verify independently [11]. Metric analysis provides little information on the mechanisms or the equations generating chaotic processes. Thus the problem of the comparison between the DOPL model (or the experimental) chaotic dynamics and that of the Lorenz model can be considered as not fully satisfactory yet.

In recent years it has been shown that a topological analysis of chaotic time series can yield more information on the mechanisms generating such behavior in a given system, thus leading to a very deep characterization of its dynamics [12–21]. In the present paper a topological analysis of the chaotic time series generated by the DOPL model is performed, with a twofold aim: (i) to provide a definitive evaluation of the degree of equivalence between the dynamics of the complex DOPL model and that of the simple Lorenz model; (ii) to study the influence of laser parameter variations on this equivalence. In particular, it is known that an increase or a decrease of the cavity losses from an optimum value leads to some differences between the DOPL chaotic pulsing (or the experimentally observed one) and the typical Lorenz model chaotic pulsing [6,8]. A double-peaked cusp in the peak-intensity return map appears, and several generalized dimensions take slightly larger values. We wish to know whether these changes represent a large or a small deviation from the Lorenz-model dynamics.

This topological analysis will be performed on several time series representing the field amplitude, accurately calculated from the DOPL model. They will correspond to different operating conditions, in particular, to different values of the cavity losses, in order to be able to investigate the differences with respect to the Lorenz model just pointed out above.

As indicated, the objective of a topological analysis is to determine the mechanism that is responsible for generating the chaotic time series. A chaotic time series is generated by two competing processes. On the one hand, most initial conditions diverge from each other. This phenomenon is usually called ''sensitive dependence on initial conditions,'' and is caused by the stretching of phase space in some direction.

On the other hand, if the motion is constrained to a bounded region in phase space, two initially nearby points cannot continue to separate from each other indefinitely. There must be some mechanism that takes distant regions in phase space and ''squeezes'' them together. The objective of topological analysis is to determine the stretching and squeezing mechanisms that operate in the appropriate phase space [12,13].

This analysis is facilitated by an observation due to Birman and Williams [14]. Their theorem states that a strange attractor in R^3 can be compressed along the stable direction without altering the topological organization of the unstable periodic orbits in the flow. After compression, the strange attractor and all the periodic orbits in it exist on a branched two-dimensional manifold. This branched manifold provides a caricature for the strange attractor. Moreover, the topological organization of all periodic orbits in the strange attractor is completely defined by this branched manifold. The objective of a topological analysis of chaotic data is the determination of the branched manifold (or template) which characterizes the attractor [15].

A branched manifold provides an important starting point for the description of physical systems that behave chaotically. As experimental parameters, or model control parameters, are varied, it is useful to regard the phase-space flow as being restricted to different parts of the branched manifold. This smooth variation of the restriction then accounts for the bifurcations that occur as parameters are changed. For any parameter values, the spectrum of periodic orbits that exists in a chaotic flow, up to any period, can be specified by a ''basis of unstable periodic orbits'' [22]. This basis provides an estimate of the system's topological entropy.

The analysis procedure has been reduced to a series of simple steps [12,13]. These are as follows. (i) Embed the data. (ii) Extract the unstable ''periodic orbits.'' (iii) Compute the topological invariants (linking numbers). (iv) Identify the branched manifold. (v) Verify this identification. This topological analysis procedure has successfully been applied to a number of experimental data sets [12,16–20].

We now carry out a topological analysis on three specific DOPL data sets, which will be denoted *A*, *B*, and *C* and correspond to the operation conditions also denoted as *A*, *B*, and *C* in Ref. [6]. In case *B* the cavity losses take an optimum value, namely, $\sigma=1.85$ (value normalized to the transverse relaxation rate of the molecular amplifying medium), for which there is a maximum coincidence, with respect to metric properties, with the Lorenz-model predictions. In cases *A* and *C*, the cavity losses are smaller ($\sigma=1.15$) and larger ($\sigma=7$), respectively, so that the possible subtle differences with respect to the Lorenz model pointed out above show up. In the three data sets the variable recorded is the real (positive or negative) amplitude of the laser field $[x(t)]$. We first carry out the analysis of data set *B*, which is described in detail in Secs. II–VII. After completing this task, we describe more briefly the results of the analysis of data sets *A* and *C* (Sec. VIII). Finally, in Sec. IX the main conclusions are summarized. As described in detail below, the results of these analyses show that the equations generate a flow topologically equivalent to the flow generated by the Lorenz equations. A definite difference between case *B* and cases *A* and *C* is identified, but it does not affect the topology of the chaotic attractor.

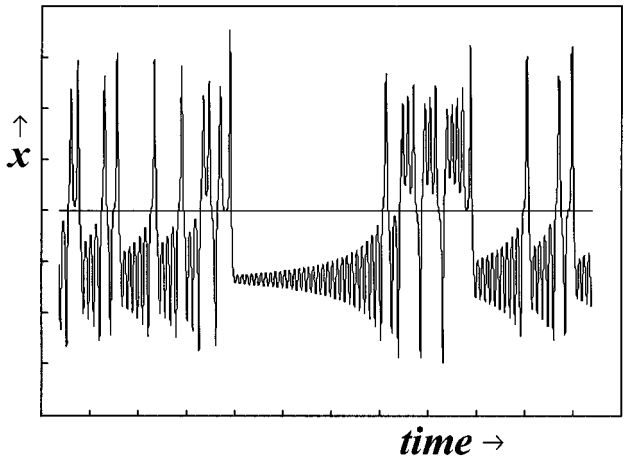

FIG. 1. Time series for a portion of data set *B* (real laser field amplitude vs time). The time separation between consecutive peaks, in absolute units, is of the order of a few microseconds.

As a complementary detail, we show in Appendix *A* how field-amplitude time series $[x(t)]$ could be obtained from field-intensity time series $[I(t)\sim x^2(t)]$. This is made because from the experimental point of view field-intensity measurements are much easier to perform than field-amplitude measurements [4].

II. VISUAL INSPECTION OF THE DATA

Even before a topological analysis is begun, useful information can be gleaned by visual inspection of the chaotic time series. A portion of the time series from data set *B*, which corresponds to the real laser field amplitude $x(t)$, is shown in Fig. 1. This variable can take positive and negative values, since the laser is assumed to operate on resonance between the molecular transition and cavity frequencies.

There appear to be two fixed points at $\pm x_0$ about which unstable oscillations take place. The observable $x(t)$ oscillates around one of these fixed points with exponentially increasing amplitude until it crosses the threshold $x=0$. Then oscillations begin about the other unstable fixed point. The larger the value of $|x(t)|$ just before the threshold is crossed, the closer the next series of exponentially growing oscillations begins around the other fixed point. We should observe here that the Lorenz system behaves in exactly this way. In fact, we will show below that the behavior of this system is essentially identical to the behavior of the Lorenz system. That is, this data set, appropriately embedded, can be smoothly deformed into the Lorenz attractor.

III. EMBEDDING

There are many ways to create an n-dimensional embedding from scalar time series data $x(i)$, $i=1,2,\ldots,T$ of length T. The default is the delay embedding method,

$$x(i)\rightarrow \mathbf{y}^d(i)=(x(i),x(i-\tau),\ldots,x[i-(d-1)\tau]), \quad (1)$$

whose principle virtues are that it is valid for any d, and all components of the embedded vectors $\mathbf{y}_j^d(i)$ have the same signal-to-noise ratio.

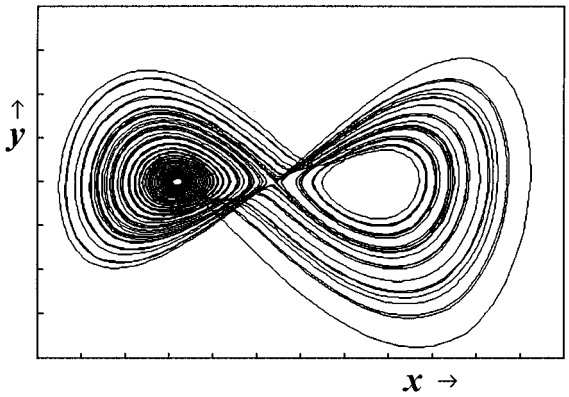

FIG. 2. Projection of the strange attractor $(x(t),y(t),z(t))$ associated with data set B onto the x-y plane. The coordinate y is defined as the derivative of x: $y=dx/dt$.

In this work we use embeddings that depend on derivatives [12,13]. Such embeddings are useful because they address questions of dynamics. They are also useful because it is a simple matter to determine linking numbers of periodic orbits simply by inspection. One serious drawback is that differentiation decreases the signal-to-noise ratio. For the data sets at hand this does not pose a problem.

In Fig. 2 we plot the projection of the strange attractor $x(t)\rightarrow(x(t),y(t),z(t))$ onto the x-y plane. In this embedding $y(t)=dx(t)/dt$. Since all crossings are transverse, the embedding is sufficient to guarantee that the uniqueness theorem of ordinary differential equations is satisfied provided we take minimal care with the definition of the coordinate $z(t)$.

One convenient choice for $z(t)$ is $dy(t)/dt$. With such an embedding the linking numbers of periodic orbits can be computed very easily. We illustrate this in Fig. 3(a). At the intersection of two orbit segments, the slope (S) of either segment is

$$S=\frac{dy}{dx}=\frac{dy/dt}{dx/dt}=\frac{z}{y},$$

$$z=yS \tag{2}$$

Therefore, in the half plane $y>0$, the larger the slope, the larger the z coordinate. The reverse is true in the half plane $y<0$. In the projection of two periodic orbits onto the x-y plane, each crossing is assigned an integer value: ± 1. The sign is determined as follows. Rotate the tangent vector to the upper segment into the tangent vector to the lower segment through the smallest possible angle. If this is done using a left-hand rule, the sign is -1. With the right hand rule, the sign is $+1$. The linking number of two periodic orbits is then half the sum over all signed crossings.

The embedding represented by $(x,y,z)=(x,dx/dt,d^2x/dt^2)$ presents two difficulties. Crossings in the upper half plane are negative while those in the lower half plane are positive. Therefore, the linking numbers of two periodic orbits is half the difference between the number of crossings in the lower half plane and the number of crossings in the upper half plane. Inspection of the standard representation of

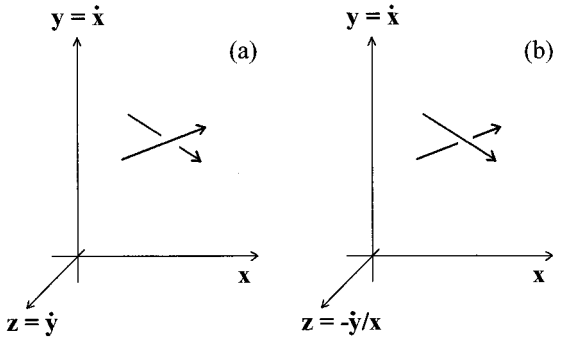

FIG. 3. Determination of linking numbers by visual inspection of the embedding. (a) For the embedding $z=dy/dt$ all crossings in the upper half plane $y>0$ are negative, by the left-hand rule. All crossing in the lower half plane are positive. (b) For the embedding with $z=-y(dy/dt)$ all crossings in the first and third quadrants, where the only crossings occur, are positive.

the Lorenz attractor in Fig. 4(a) shows that all crossings are positive. The second difficulty is that the Lorenz system has a rotation symmetry. It is invariant under rotation through π radians about the z axis: $R_z(\pi)\ (x,y,z)=(-x,-y,+z)$. It is not clear from inspection of Fig. 2 that the strange attractor that we are analyzing has any symmetry at all. If it is in fact symmetric, it may exhibit lack of symmetry by accident of initial conditions or by the finite length of the data set plotted. [In Sec. VII we show convincingly that it is symmetric under $(x,y)\rightarrow(-x,-y)$]. However, if there is a symmetry under $(x,y)\rightarrow(-x,-y)$, it is an inversion symmetry under the embedding (2):

$$P(x,y,z)\rightarrow(-x,-y,-z) \tag{3}$$

because of the way in which $z=dy/dt$ is defined.

If we wish to show equivalence between the data set under study and the Lorenz system, we must choose a different embedding. Such an embedding should possess the same symmetry as the Lorenz attractor [e.g., $R_z(\pi)$] and should generate only positive crossings. Such an embedding is

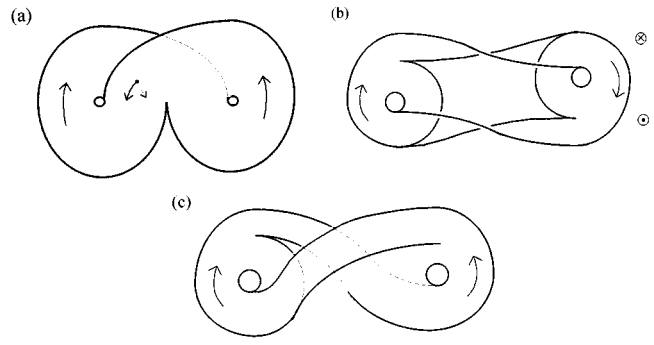

FIG. 4. (a) Schematic representation of the Lorenz attractor. All crossings are positive. (b) Schematic representation of the attractor constructed from data set B using the embedding (4). (c) When the attractor shown in (b) is deformed by rotating the right-hand lobe through π radians, top into the page, it is easily recognizable as topologically equivalent to the Lorenz attractor.

$$\dot{x}=y,$$

$$y\dot{y}=-z, \tag{4}$$

$$\dot{z}=f(x,y,z).$$

The crossing convention is shown in Fig. 3(b). By the previous argument, at a crossing

$$z=(-y^2)S, \tag{5}$$

where S is again dy/dx. For $y\neq 0$, the larger the slope, the more negative the coordinate z. As a result, all crossings are positive. In addition, if the strange attractor exhibits a symmetry, it is of the correct type:

$$R_z(\pi)(x,y,z)\rightarrow(-x,-y,+z). \tag{6}$$

For this embedding, determining the dynamics becomes a problem of determining the single function $f(x,y,z)$.

IV. PRELIMINARY IDENTIFICATION OF BRANCHED MANIFOLDS

Before proceeding with the topological analysis, we present a simple argument to show that the strange attractor generated by data set B, using the embedding (4), should be equivalent to the Lorenz attractor. In Fig. 4(b) we provide a schematic representation of the strange attractor. The flow from the left lobe to the right lobe in the upper half plane ($y>0$) exhibits a half twist with a clockwise rotation in the direction of the flow. This branch of the flow is joined to the circular flow in the right-hand lobe from the top. The same is true, by $R_z(\pi)$ symmetry, for the flow from the right-hand lobe to the left-hand lobe in the lower half plane. If the right-hand lobe is given a rotation by π radians about the positive x axis, with the top into ($\otimes$) the x-y plane and the bottom out ($\odot$), as shown, then Fig. 4(c) is a caricature of the flow. This is easily seen to be equivalent to the Lorenz flow, shown in Fig. 4(a).

V. PERIODIC ORBITS

The next step in the topological analysis involves extraction of unstable periodic orbits from the chaotic time series data. Unstable periodic orbits exist in abundance in a strange attractor. In fact, they are dense in a hyperbolic strange attractor.

When the point representing the state of a system falls into the neighborhood of an unstable periodic orbit of sufficiently low period, it may evolve in the neighborhood of that orbit until it returns to the neighborhood of its starting point. It then evolves along a path in phase space very close to an earlier part of its trajectory. This recursion of evolution in phase space provides a tool by means of which segments of the trajectory that shadow unstable periodic orbits may be recognized [12,13,17].

There are in fact no segments of the time series data that *are* unstable periodic orbits. However, many segments of the data track unstable periodic orbits sufficiently closely for sufficiently long that they can be recognized and then used as surrogates for these orbits. These segments of the chaotic time series can be identified by the method of close returns. We have used this method to locate many unstable periodic orbits in data set B. To period six, we have identified the following 15 orbits, named by their symbolic dynamics: LR; L^2R, LR^2; L^3R, LR^3, L^2R^2; L^4R, LR^4, L^3R^2, $LRLR^2$; L^5R, LR^5, L^4R^2, L^2R^4, $LRLR^3$. In addition, the fixed points at $(\pm x_0,0,0)$ are effectively the period-one unstable periodic orbits L,R.

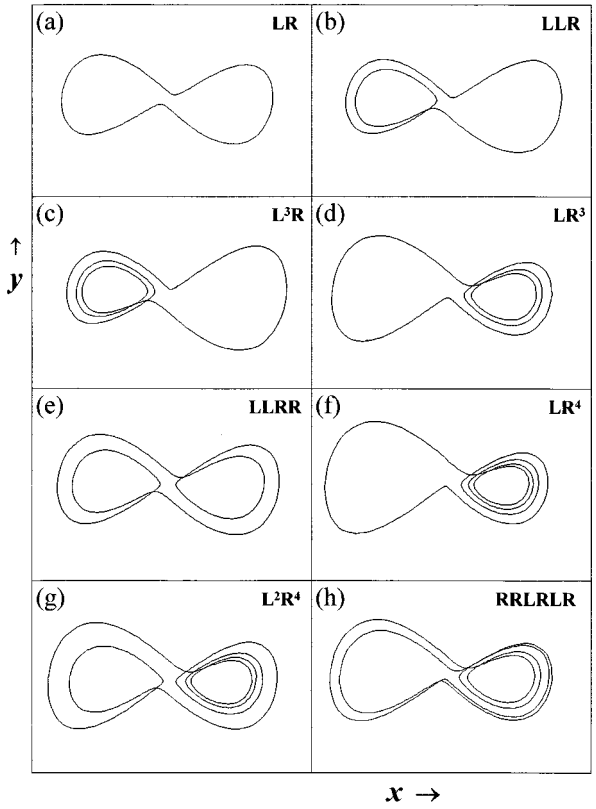

FIG. 5. A selection of unstable periodic orbits extracted from data set B by the method of close returns.

Several of these orbits are shown in Fig. 5. None of these orbits actually closes. However, to the resolution shown, they all appear closed.

VI. IDENTIFICATION OF THE TEMPLATE

The template, or branched manifold, that characterizes a strange attractor can be described in an invariant way by a topological index. This is simply a set of integers. These integers are determined from the period-one and period-two orbits (L,R,LR). The properties of these orbits determine a 2×2 template matrix and a 1×2 reconnection array. The template matrix consists of the self-linking and linking numbers of the period-one orbits. Since these orbits are points, they do not link and their self-linking numbers are zero. The template matrix is

$$\begin{bmatrix} 0 & 0 \\ 0 & 0 \end{bmatrix},$$

$$[+1-1]. \tag{7}$$

TABLE I. Linking numbers for all orbits up to period six extracted from data set B by the method of close returns. All linking numbers were computed from the data and from the Lorenz template. The self-linking numbers (on diagonal) were computed from the Lorenz template but not from the data.

	1	2	3	4	5	6	7	8	9	10	11	12	13	14	15
LR	1	1	1	1	1	2	1	1	2	2	1	1	2	2	2
L^2R	1	2	1	2	1	2	2	1	3	2	2	1	3	2	2
LR^2	1	1	2	1	2	2	1	2	2	3	1	2	2	3	4
L^3R	1	2	1	3	1	2	3	1	3	2	3	1	4	2	2
LR^3	1	1	2	1	3	2	1	3	2	3	1	3	2	4	4
L^2R^2	2	2	2	2	2	3	2	2	3	4	2	2	3	3	4
L^4R	1	2	1	3	1	2	4	1	3	2	4	1	4	2	2
LR^4	1	1	2	1	3	2	1	4	2	3	1	4	2	4	4
L^3R^2	2	3	2	3	2	3	3	2	4	4	3	2	4	3	4
$LRLR^2$	2	2	3	2	3	4	2	3	4	6	2	3	4	5	6
L^5R	1	2	1	3	1	2	4	1	3	2	5	1	4	2	2
LR^5	1	1	2	1	3	2	1	4	2	3	1	5	2	4	4
L^4R^2	2	3	2	4	2	3	4	2	4	4	4	2	5	3	4
L^2R^4	2	2	3	2	4	3	2	4	3	5	2	4	3	5	6
$LRLR^3$	2	2	4	2	4	4	2	4	4	6	2	4	4	6	7

The reconnection array determines whether the branches are connected from above or below, in the projection used. The larger the integer, the further behind the branch is when the connection occurs. Since the right-hand branch joins the left-hand branch from the top [Fig. 4(c)], the array is $[+1,-1]$. The topological characterization of the Lorenz template is given by Eq. (7) [12,13,15].

In order to verify this identification, we have computed the linking numbers for all pairs of unstable periodic orbits ($p \leqslant 6$) extracted from the chaotic time series. This was easily done by superposing the orbits and counting the total number of crossings. This even number is twice the linking number of the orbit pair [21]. The results are presented in Table I. These linking numbers were also computed for the corresponding orbits in the Lorenz template. The linking numbers computed from the data, and calculated for the Lorenz template, were identical.

VII. SYMMETRY

We now return to the question of whether the strange attractor possesses a symmetry. Figure 2 presents a projection of a segment of the time series data onto the x-y plane. This projection does not convincingly suggest the presence of symmetry under $(x,y) \rightarrow (-x,-y)$. This may be because there is in fact no symmetry. Or it may be because we have not plotted a sufficiently long segment of chaotic data.

To unambiguously resolve this question, it is sufficient to compare the unstable periodic orbits extracted from the data. Under rotation symmetry

$$R_z(\pi): \quad L \rightarrow R, \quad R \rightarrow L \tag{8}$$

Thus, the rotated image of L^2R will be indistinguishable from R^2L if the attractor is $R_z(\pi)$ symmetric. If the attractor lacks rotational symmetry, these orbits will be distinguishable.

We have compared all unstable periodic orbits extracted from the data that should be related by symmetry. These include

$$\begin{gathered} LR \leftrightarrow RL \quad \text{(self)}, \\ L^2R \leftrightarrow R^2L, \\ L^3R \leftrightarrow R^3L, \\ L^2R^2 \leftrightarrow R^2L^2 \quad \text{(self)}, \\ L^4R \leftrightarrow R^4L, \\ L^5R \leftrightarrow R^5L, \\ L^4R^2 \leftrightarrow R^4L^2. \end{gathered} \tag{9}$$

In every case, the rotated image of one orbit was identical to its counterpart [see, for instance, Figs. 5(c) and 5(d)]. In two cases (LR, L^2R^2) the rotated image was identical to the original. We therefore feel safe in concluding that the strange attractor generated by data set B, with embedding (4), exhibits the topological structure of the Lorenz attractor and is invariant under $R_z(\pi)(x,y,z) \rightarrow (-x,-y,+z)$.

VIII. DATA SETS *A* AND *C*

An identical analysis has been carried out on data set A. We will not review the entire analysis. Rather, we will point out where slight differences exist.

Data set A corresponds to a small value of the cavity losses ($\sigma = 1.15$), for which the ''bad cavity'' condition $\sigma < b+1$ is no longer verified ($b = 0.28$ for the NH_3 laser). This implies that the steady state remains stable for any pumping strength (the subcritical Hopf bifurcation affecting it at a finite value of the pump strength in case B has now shifted toward an infinite value of the pumping strength). The chaotic dynamics can nevertheless be obtained by hard-

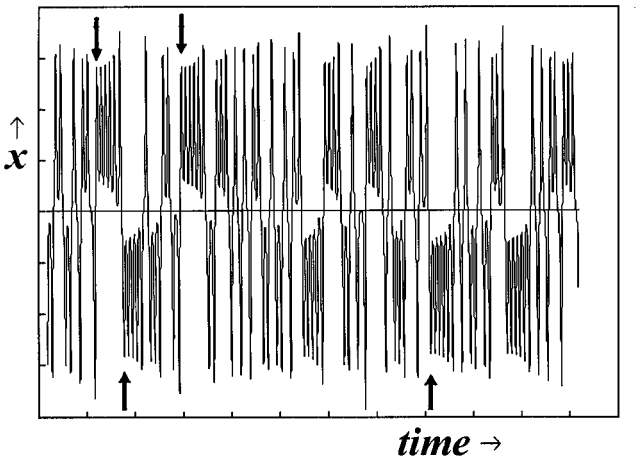

FIG. 6. Time series for a portion of data set A. Arrows indicate where monotonicity is lost.

mode excitation (i.e., by a finite-amplitude perturbation of the steady state).

Visual inspection of data set A (Fig. 6) reveals two ways in which it differs from data set B. First, there do not appear to be fixed points in the data set. Rather, the smallest oscillations appear to be unstable period-one limit cycles in the left ($x<0$) and right ($x>0$) lobes. We might therefore expect to be able to extract real period one orbits (L,R) from the data by the method of close returns (cf. Fig. 8 below). Second, on transition through the threshold $x=0$, monotonicity is lost. That is, it is no longer true that the larger the amplitude $|x|$ just before transition from $x<0$ to $x>0$ (or *vice versa*), the smaller the amplitude of oscillation around the new limit cycle. A few such instances are indicated by arrows in Fig. 6. In fact, the more x overshoots on the transition, the smaller the amplitude on the next oscillation, and the nearer it gets to the unstable limit cycle. These facts (in particular, the fact that the first peak in each growing spiral sequence can be slightly larger than the next peak) are related to the appearance of a double-peaked cusp in the peak-intensity return map [7,8].

In Fig. 7(a) we present a projection of the strange attractor onto the x-y plane, where as before $y=dx/dt$. This schematic representation indicates the extra twist introduced into the flow by the nonmonotonicity. In Fig. 7(b) we show the limit cycle, its stable manifold (vertical), and unstable manifold (horizontal annulus). When a point overshoots, it approaches the limit cycle along the stable manifold and then spirals away from it along the unstable manifold. A point that does not overshoot settles into the unstable manifold, but not as close to the limit cycle, and then spirals away. The nonmonotonicity in the data is due entirely to the outward leaning structure of the unstable manifold. If this is deformed to lean inward, the nonmonotonicity disappears. Crossings in the projection to the x-y plane are pushed from the second and fourth quadrants into the third and first quadrants without changing their sign. The topological organization of all unstable periodic orbits remains unchanged. The dynamics is clearly Lorenz-like. The only difference is that the unstable fixed points are replaced by unstable periodic orbits of period 1. The sequence of deformations shown in Fig. 4, which takes the strange attractor for data set B into the Lorenz

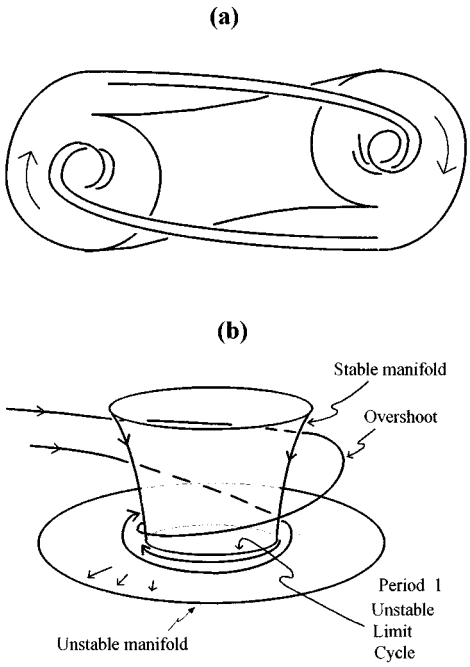

FIG. 7. Projection of the strange attractor $(x(t),y(t),z(t))$ associated with data set A onto the x-y plane. The coordinate y is defined as the derivative of x: $y=dx/dt$. This projection shows an extra twist not observed in Fig. 2. This twist can be unwound smoothly without disorganizing any of the unstable periodic orbits.

attractor, can then be applied to data set A.

We have extracted unstable periodic orbits from data set A by the method of close returns. To period 6, the 19 unstable periodic orbits we have extracted are: L, R; LR; L^2R, LR^2; L^3R, LR^3, L^2R^2; L^4R, LR^4, L^2RLR, R^2LRL, L^3R^2, L^2R^3; L^5R, LR^5, L^3RLR, R^3LRL, L^2R^2LR. Several of these orbits are shown in Fig. 8. We could not find the orbits L^4R^2 and R^4L^2 to the precision used to find the other orbits. The linking numbers for all orbit pairs were computed, and all agreed with the linking numbers for corresponding orbits for the standard Lorenz template.

To determine whether the strange attractor for data set A is symmetric, we compared mirror image orbit pairs. Ten such comparisons were made on the 19 unstable periodic orbits extracted from data set A. In each case, the rotated image of one orbit was indistinguishable from the mirror image orbit [see, for instance, Figs. 8(c) and 8(d)].

We therefore conclude that the strange attractor generated by data set A with the embedding (4) exhibits the topological structure of the Lorenz attractor. It is also invariant under $R_z(\pi)(x,y,z)\rightarrow(-x,-y,+z)$. The two strange attractors, from data sets B and A, can be deformed into each other. The deformation is smooth except for the Hopf bifurcation, which separates one from the other. This bifurcation replaces the unstable fixed points, which are present in data set B with the unstable period-one limit cycles, which appear in data set A.

At variance with data set A, data set C corresponds to large cavity losses ($\sigma=7$), for which the system is well inside the ''bad cavity'' limit. In these conditions, we have found that the subcritical Hopf bifurcation affecting the

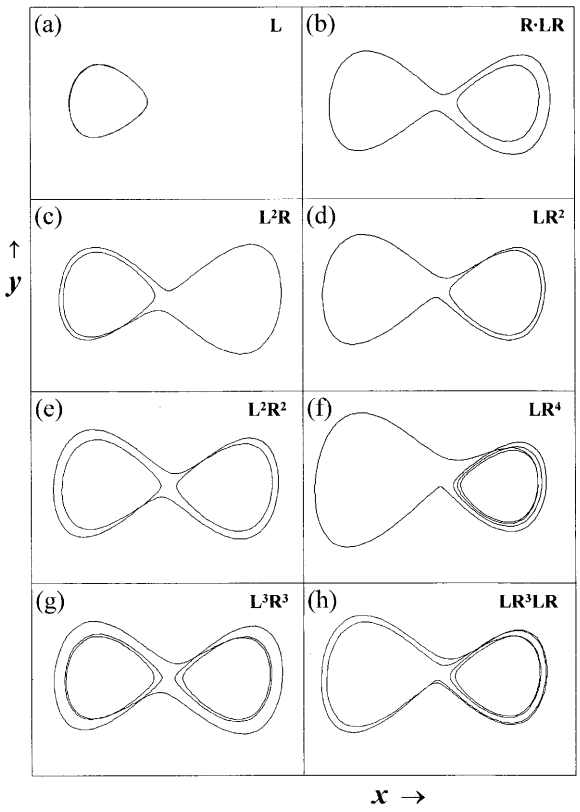

FIG. 8. A selection of unstable periodic orbits extracted from data set A by the method of close returns.

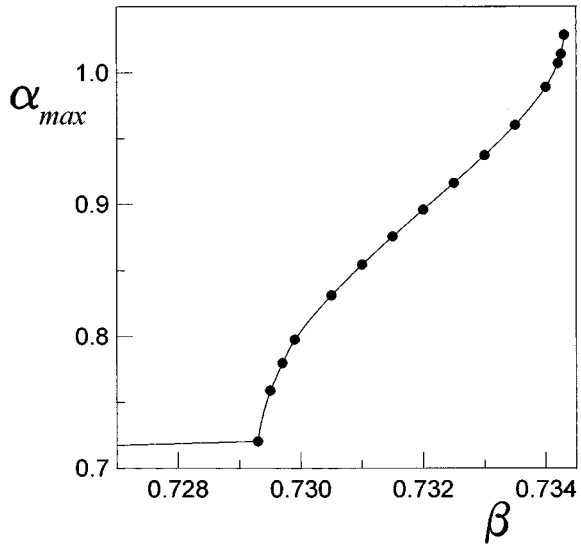

FIG. 9. Maximum amplitude of the laser field ($\alpha_{\max}$) as a function of the pump field amplitude β. For $\beta<0.7293$ the laser field emission is stable. At $\beta=0.7293$ a supercritical Hopf bifurcation occurs, so that for $\beta>0.7293$ the emission is modulated in time. 2α and 2β represent the Rabi frequencies of the laser and pump fields, respectively, in units of the molecular transverse relaxation rate.

steady state in the case of data set B or in the Lorenz model now becomes supercritical, as shown in Fig. 9. A stable limit cycle appears in phase space, which by further increasing pumping strength soon becomes unstable and chaos is reached. Figure 10 shows the phase-space plot of dx/dt versus $x(t)$ for data set C. These phase-space plots are essentially indistinguishable from the phase-space plots constructed from data set A. The two phase-space plots are topologically identical. We have extracted 16 unstable periodic orbits from the field amplitudes recovered from data set C: L, R; LR; L^2R, R^2L; L^2R^2, L^3R, R^3L; L^4R, R^4L, L^2RLR, R^2LRL, L^3R^2; L^5R, R^2L^2RL, R^3LRL. The attractor obtained from data set C is symmetric by the usual tests on symmetry related orbits.

Data sets B, A, and C represent laser field amplitudes $x(t)$, which can take positive and negative values. However, experimentally it is much easier to obtain laser field intensities $I(t)\sim x^2(t)$ [4]. In the Appendix we show how a field amplitude time series could be extracted from a recorded field intensity time series, when necessary [a topological analysis to recover the underlying dynamics cannot be carried out directly on $x^2(t)$ data].

IX. CONCLUSIONS

We have carried out a topological analysis on several data sets generated by the Doppler broadened optically pumped laser model, which involves six parameters and up to several hundred first-order differential equations. For each data set the dynamics is reducible to that of a three-dimensional dynamical system. With appropriate phase-space embedding the dynamics is seen to be topologically equivalent to that of the Lorenz system.

In each case the analysis involved several steps. (i) Embed the data. (ii) Extract the unstable periodic orbits. (iii) Compute the topological invariants (linking numbers). (iv) Identify the branched manifold. (v) Verify this identification.

Many embeddings are possible. To show the similarity with the Lorenz system we used the differential phase-space embedding (4), which respects the rotation symmetry under $R_z(\pi)$ (3) of the Lorenz system. The unstable periodic orbits were extracted by the method of close returns. For each of the data sets analyzed we were able to extract more than a dozen unstable periodic orbits. The topological invariants (linking numbers) were computed simply by ''counting

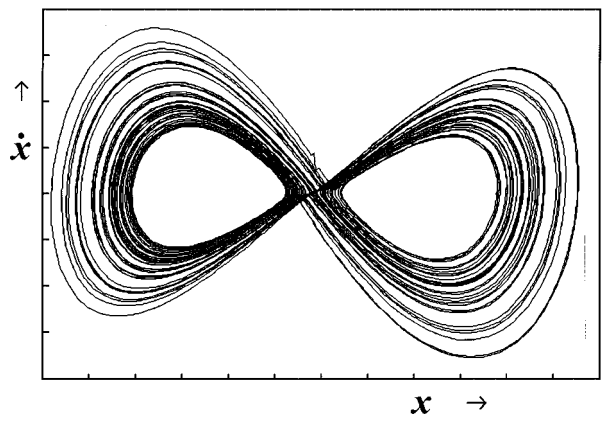

FIG. 10. Phase-space plot dx/dt vs $x(t)$. This phase-space plot is topologically equivalent to that constructed from the amplitude data in data set A.

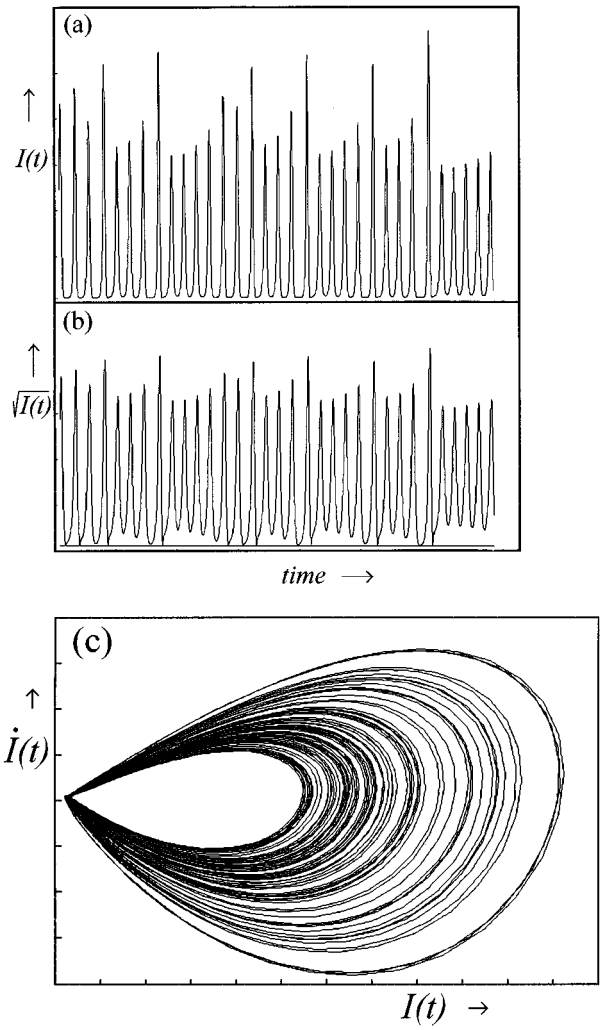

FIG. 11. (a) Intensity $I(t)$ vs time t for part of data set C. The time separation between consecutive peaks, in absolute units, is of the order of a few microseconds. (b) Morphology of the minima of $I(t)^{1/2}$ vs t for the intensity data shown in (a). (c) Phase-space plot dI/dt vs $I(t)$ for this time series.

crossings.'' An underlying template was then identified using a subset of the orbits extracted. In each case, the underlying template was that of the classical Lorenz attractor. This is defined algebraically by a set of integers (7). This algebraic characterization was then used to predict the linking numbers of all other unstable periodic orbits extracted from the data. In this way we were able to validate our original template identification.

The topological analysis procedure was applied directly to data sets B, A, and C, which measured the field amplitudes.

Data set B exhibits two fixed points in the phase-space projection ($\dot{x}$ versus x) at $(x,\dot{x})=(\pm x_0,0)$. These fixed points are weakly unstable foci. They are separated by a saddle at the origin. Data set A differs from data set B by a pair of symmetry related Hopf bifurcations. The fixed points at $(\pm x_0,0)$ are inaccessible: they are surrounded by unstable limit cycles, as can be seen in Fig. 7. Data set C has been shown to be topologically identical to data set A, with the Hopf bifurcation being supercritical instead of subcritical.

Thus, we finally conclude that the embedded data sets are topologically equivalent to the Lorenz attractor. This definitely confirms the predictions of previous metric analyses, in the sense that an optically pumped far-infrared gas laser behaves, in spite of its larger complexity, as the Lorenz model. This occurs especially for a certain domain of parameter values (that associated to data set B). Decreasing (data set A) or increasing (data set C) laser cavity losses introduces some small definite changes in the phase-space structure (trajectories approach a limit cycle instead of a fixed point; supercritical Hopf bifurcation in case C). The first of these changes could also be found in the Lorenz model by scanning its three parameters r, σ, and b (although the sensitivity to these parameter variations is not the same in both models), but the second change probably could not be found (the Lorenz equations do not provide a complete unfolding of the most general dynamics that could appear in a phase space with two saddle foci separated by an unstable regular saddle). However, from the point of view of the branched manifold associated to the chaotic attractor, this does not represent any topological difference.

ACKNOWLEDGMENTS

Partial support from the Spanish Dirección General de Investigación Científica y Técnica (DGICYT) through Projects PB92-0600 and PB95-0778 is acknowledged.

APPENDIX

To show how a field amplitude time series could be extracted from a recorded field intensity time series, we have recalculated data set C recording only the field intensity [Fig. 11(a)]. From it, the field amplitude time series has been reobtained in the following way.

First, $dI(t)/dt$ is plotted versus $I(t)$ [Fig. 11(c)]. The almost degenerate set of crossings near the origin can be expanded by a logarithmic transformation. In fact, $d(\log I)/dt$ versus $\log I$ has the appearance of a Rössler attractor.

In order to recover amplitudes from intensity data, we must take the square root of the data, paying careful attention to sign changes. It is clear that the amplitude can undergo a sign change only at an intensity minimum. However, only some intensity minima are caused by an amplitude zero

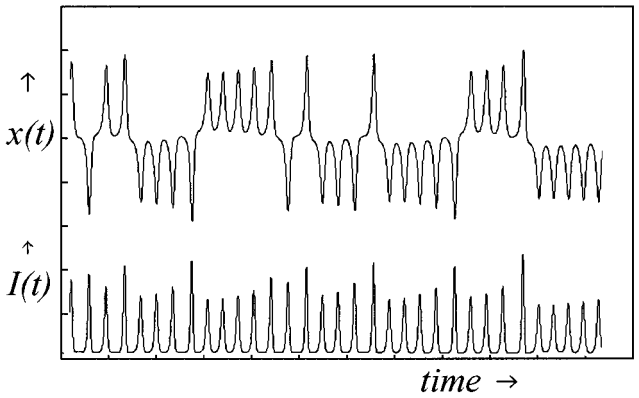

FIG. 12. Field-amplitude data $x(t)$ vs t (top) recovered from the intensity data (bottom) of data set C using the algorithm described in the text.

crossing. To separate the two, it is useful to plot $\sqrt{I(t)}$ versus t [Fig. 11(b)]. If I_0 represents a local intensity minimum, then intensities near that minimum can be represented as $I(t)=[I(t)-I_0]+I_0 = I_0+\Delta I(t)$. Since $x^2(t)=I(t)$, we have

$$|x(t)|=\sqrt{I_0+\Delta I(t)}=\begin{cases}\sqrt{I_0}+(1/2\sqrt{I_0})\Delta I(t) & \text{for } I_0\neq 0\\ \sqrt{\Delta I(t)} & \text{for } I_0=0.\end{cases} \tag{A1}$$

In the first case, $|x(t)|=\sqrt{I(t)}$ has a parabolic minimum. In the second case, which involves a zero crossing of the amplitude, $|x(t)|$ approaches and departs linearly from the x axis. This morphology can be used to locate zero crossings of the field amplitude.

Recovery of the field amplitude from the intensity was implemented using a slightly more sophisticated procedure. First, an integer l $(=\pm 1)$ was defined. This integer determines which of the two square roots $x(t)$ $=\pm\sqrt{I(t)}=l\sqrt{I(t)}$ should be taken. Then the time derivatives in two successive time intervals (with and without sign changes) were compared according to

$$x3=l\sqrt{I_{i+1}},$$

$$S1=|(+x3-x2)-(x2-x1)|, \tag{A2}$$

$$S2=|(-x3-x2)-(x2-x1)|.$$

After each comparison we cycle the variables according to $x2\rightarrow x1$, $x3\rightarrow x2$, and continue. Normally $S1<S2$ and the amplitude does not undergo a sign change. Whenever the amplitude does undergo a sign change, $S1>S2$. Under this condition, we make the replacements $x3\rightarrow -x3$, $l\rightarrow -l$, and continue. This algorithm very effectively determines the amplitude zero crossings. In Fig. 12 we plot $x(t)$, recovered from $I(t)$ using this algorithm, versus t. We have verified that this result for $x(t)$ coincides with the one that is directly obtained from direct numerical resolution of the laser equations, with almost no discrepancy along the time series (in the case of experimental data sets, the presence of noise could probably introduce some alterations in the sign of the fields at some instants of time).

[1] C. O. Weiss and R. Vilaseca, *Dynamics of Lasers* (VCH, Weinheim, Germany, 1991); N. B. Abraham, P. Mandel, and L. M. Narducci, Prog. Opt. **25**, 1 (1988); *Instabilities and Chaos in Quantum Optics*, edited by F. T. Arecchi and R. G. Harrison (Springer, Berlin, 1987).

[2] H. Haken, Phys. Lett. A **53**, 77 (1975).

[3] E. N. Lorenz, J. Atmos. Sci. **20**, 130 (1963).

[4] C. O. Weiss, N. B. Abraham, and U. Hübner, Phys. Rev. Lett. **61**, 1587 (1988).

[5] C. O. Weiss and W. Klische, Opt. Commun. **51**, 47 (1984); C. O. Weiss and J. Brock, Phys. Rev. Lett. **57**, 2804 (1986).

[6] See discussion in: E. Roldán, G. J. de Valcárcel, R. Vilaseca, R. Corbalán, V. J. Martínez, and R. Gilmore, Quant. Semiclass. Opt. (to be published).

[7] R. Corbalán, F. Laguarta, J. Pujol, and R. Vilaseca, Opt. Commun. **71**, 290 (1989); G. J. de Valcárcel, E. Roldán, and R. Vilaseca, J. Opt. Soc. Am. B **8**, 2420 (1991).

[8] C. O. Weiss, R. Vilaseca, N. B. Abraham, R. Corbalán, E. Roldán, G. J. de Valcárcel, J. Pujol, U. Hübner, and D. Y. Tang, Appl. Phys. B **61**, 223 (1995).

[9] P. Grassberger and I. Procaccia, Physica D **9**, 189 (1983).

[10] P. Grassberger and I. Procaccia, Phys. Rev. A **28**, 2591 (1983).

[11] X.-J. Hou, R. Gilmore, G. B. Mindlin, and H. G. Solari, Phys. Lett. A **151**, 43 (1990).

[12] G. B. Mindlin, H. G. Solari, M. A. Natiello, R. Gilmore, and X.-J. Hou, J. Nonlin. Science **1**, 147 (1991).

[13] G. B. Mindlin and R. Gilmore, Physica D **58**, 229 (1992).

[14] J. S. Birman and R. F. Williams, Topology **22**, 47 (1983).

[15] G. B. Mindlin, X.-J. Hou, H. G. Solari, R. Gilmore, and N. B. Tufillaro, Phys. Rev. Lett. **64**, 2350 (1990).

[16] H. G. Solari and R. Gilmore, Phys. Rev. A **38**, 1566 (1988).

[17] N. B. Tufillaro, H. G. Solari, and R. Gilmore, Phys. Rev. A **41**, 5717 (1990).

[18] R. Gilmore and J. W. L. McCallum, Phys. Rev. E **51**, 935 (1995).

[19] F. Papoff, A. Fioretti, E. Arimondo, G. B. Mindlin, H. G. Solari, and R. Gilmore, Phys. Rev. Lett. **68**, 1128 (1992).

[20] P. T. Boyd, G. B. Mindlin, R. Gilmore, and H. G. Solari, Astrophys. J. **431**, 425 (1994).

[21] H. G. Solari and R. Gilmore, Phys. Rev. A **37**, 3096 (1988).

[22] G. B. Mindlin, R. López-Ruiz, H. G. Solari, and R. Gilmore, Phys. Rev. E **48**, 4297 (1993).